Multi-stability of the hexagonal origami hypar based on group theory and symmetry breaking

Yao Chen, Ruizhi Xu, Chenhao Lu, Ke Liu, Jian Feng, Pooya Sareh

Multi-stability of hexagonal origami hypar based on group theory and symmetry breaking

Yao Chen , Ruizhi Xu , Chenhao Lu , Ke Liu , Jian Feng , Pooya Sareh

PII: S0020-7403(23)00098-X
DOI: https://doi.org/10.1016/j.ijmecsci.2023.108196
Reference: MS 108196

To appear in: *International Journal of Mechanical Sciences*

Received date: 19 November 2022
Revised date: 30 January 2023
Accepted date: 30 January 2023

Please cite this article as: Yao Chen , Ruizhi Xu , Chenhao Lu , Ke Liu , Jian Feng , Pooya Sareh , Multi-stability of hexagonal origami hypar based on group theory and symmetry breaking, *International Journal of Mechanical Sciences* (2023), doi: https://doi.org/10.1016/j.ijmecsci.2023.108196

Multi-stability of hexagonal origami hypar based on group theory and symmetry breaking

Yao Chen [a*], Ruizhi Xu [a], Chenhao Lu [a], Ke Liu [b], Jian Feng [a], Pooya Sareh [c, d]

[a] Key Laboratory of Concrete and Prestressed Concrete Structures of Ministry of Education, and National Prestress Engineering Research Center, Southeast University, Nanjing 211189, China

[b] Department of Advanced Manufacturing and Robotics, Peking University, Beijing 100871, China

[c] Creative Design Engineering Lab (Cdel), Department of Mechanical and Aerospace Engineering, School of Engineering, University of Liverpool, Liverpool, L69 3GH, United Kingdom

[d] Escuela Técnica Superior de Ingeniería y Diseño Industrial, Universidad Politécnica de Madrid (UPM), Madrid 28040, Spain

Highlights

Kinematic analysis of origami can be simplified by group theory and symmetry breaking.

Hexagonal origami hypar exhibits one critical point and six stable states in three bifurcation branches.

Folding of hexagonal origami hypar is mainly affected by crease folding and panel bending deformation.

Energy barrier among all stable states of hexagonal origami hypar increases with higher symmetry.

* Corresponding author, Email: chenyao@seu.edu.cn

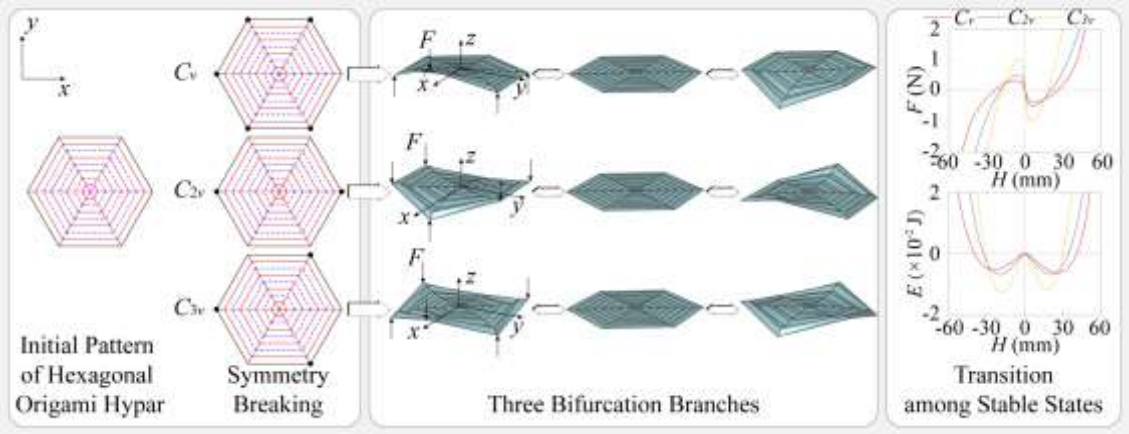

Abstract: Origami hyperbolic paraboloid (origami hypar) is widely known for its characteristic non-zero Gaussian curvature and multi-stable states. Previous investigations have concerned two particular cases of the origami hyper patterns: the square and circular ones. As a representative example of general polygonal hypar patterns, the hexagonal origami hypar displays much richer and subtler multi-stable energy and configurations, which is however, rarely studied. In this work, we investigate the multi-stability of hexagonal origami hypar by combining a group-theoretic approach, symmetry breaking method and bar-and-hinge model, to simplify the kinematic analysis of origami structures with higher-order symmetry. The whole kinematic path of the hexagonal origami hypar is divided into three bifurcation branches by symmetry breaking. Each branch corresponds to two symmetric stable states according to the equilibrium load and potential energy simulated by bar-and hinge model. The non-rigid deformation of the hexagonal origami hypar is mainly controlled by the folding of the creases and the bending of the panels. Moreover, the energy barrier among the stable states becomes increasingly stronger with higher symmetry order, thicker material thickness, and longer crease lengths. This work provides a new strategy for analyzing the multi-stable origami with high symmetry order, which is useful in the design and application of novel engineering structures.

Keywords: Origami hypar; Multi-stability; Group theory; Bifurcation; Symmetry breaking

1 Introduction

Multi-stable systems possess non-trivial energy landscapes that leads to different stable configurations. Recently, accompanied by this transition of systems between different stable states, they are increasingly adopted in bionics [1, 2], metamaterials [3, 4], robotics [5, 6], engineering structures [7, 8] and other fields. Typical multi-stable systems are designed by combining bistable units [9]. The local properties and combination of these units have critical impact on the global properties of the multi-stable system. For example, a well-assembled double-layer Kresling tube can achieve the same total height in two different stable states [10]. The rich mechanics of origami structures provide many candidates for such bistable units and have been a main source of inspiration for the design of multi-stable structures, such as Kresling configurations with different stable-state numbers [11], Kresling assembly [12, 13], and Kirigami-based metastructures [14].

A number of multi-stable origami structures are derived from traditional origami patterns, such as the Miura-ori [15-17], Tachi-Miura polyhedron [18, 19], Waterbomb tubes [20, 21], and Kresling tubes [22, 23]. By combining multi-stable origami units, such as the square twist [24, 25], leaf-like origami [26], origami-inspired cellular [27, 28], and origami hypar [29], we can get much more number of stable states and richer programmability of origami structures. To fold smoothly in the whole process, kinematics analysis is the key to the multi-stability of origami [30]. The existing methods for kinematic analysis of rigid or non-rigid origami can be divided into two types, including mechanism analysis and structural analysis. The conditions of rigid folding are more severe than that of non-rigid folding, so the kinematic analysis of rigid folding is simpler and more suitable for more computational models [31]. Kinematic of rigid origami can be simulated by means of mechanism analysis, such as polygonal surfaces [32] and spherical polygonal linkages [33], and structural analysis, such as bar-and-hinge

model [34] and shell model [35]. However, the non-rigid folding introduces the deformation of the panel, which greatly increases the variables to be considered [36]. Thus, for non-rigid origami, mechanism analysis method is not applicable for the deformation of the panels. The common analytical methods for non-rigid origami are the bar-and-hinge model with elastic bars for the tension and compression of the panel and rotating springs for the bending of the panel [37, 38], the membrane-and-hinge model with elastic membrane for the tension and compression and rotating springs for the bending [39], and thin plate element [40].

Notably, as one of the non-rigid and multi-stable origami units, origami hypar is composed of concentrically pleated polygons with a minimum of four sides [41]. Among this family of patterns, the two extreme cases have been widely studied, namely, the square origami hypar [42] and the circular origami hypar (i.e., polygon with infinite number of sides) [43, 44]. The square origami hyper has two stable states that are macroscopically symmetric with a rotation of 90 degrees [29]. When transitioning from one stable state to the other, it first unfolds to a flat state and then refold up, going through a significant energy barrier caused by the competing folding, bending, and stretching energy [37]. Moreover, the folding angle of square origami hyper can be achieved by controlling the creases' defect [45]. Namely, the creases' defect can be controlled according to the requirement to make the square origami hyper reach the proper stable state. On the other hand, the circular origami hypar can reach different stable sates under different approximate width of conditions [46]. In the simplest condition, it forms a saddle-like shape. Nevertheless, except for these two extreme cases, the multi-stability of polygonal origami hypar is still not studied in-depth. Thereafter, we will present a thorough investigation of the multi-stable behavior of the hexagonal origami hypar.

The identification of all stable states is essential to study multi-stability of hexagonal origami hypar, as

it has been experimentally observed to possess more than two stable states. Since the tangent stiffness matrix may become ill-conditioned, simulating the global properties of hexagonal origami hypar by the same method as solving the bistability may be infeasible. Therefore, the simulation of the global process needs to be simplified as the kinematic bifurcation analysis of deployable structures [47]. Bifurcations can be determined by singular value decomposition [48]. Thereafter, some numerical and robust algorithms have been applied to the geometric, kinematic, or mechanical analysis of origami structures, including geometric-graph-theoretic method [49], particle swarm optimization method [50], and mixed-integer linear programming method [51]. Another part of studies has simplified multi-stability analysis of systems by bifurcation branches, such as assuming the bifurcation parameters [52, 53] and the group theoretic approach [54, 55]. The group theoretic approach is mature in solving the bifurcation branches. Particularly, for structures with high-order symmetry, it can be simplified according to group theory [56, 57]. Based on these theories, Chen et al. [58, 59] developed a group-theoretic approach for the kinematic behavior of deployable bar structures with cyclic symmetry. However, few applications of group theory and symmetry have been implemented for origami structures.

Here, using group theory and its representations, we will propose a new strategy to study the multi-stability of hexagonal origami hypar. The group-theoretic approach is introduced to simplify the whole folding process of origami structures. The bifurcation branches of origami structures with high-order symmetry as hexagonal origami hypar can be solved by symmetry breaking. The corresponding stable states can be obtained by kinematic analysis with bar-and-hinge models of different bifurcation branches. The bifurcation branches and the corresponding stable states will reflect the multi-stability in the whole kinematic process. Moreover, our work will demonstrate the effect of material properties on

the multi-stability of this structure. This article is organized as following. Section 2 introduces the group-theoretic method for multi-stability analysis. Then, Section 3 shows the multi-stability of the hexagonal origami hypar in different bifurcation branches. Section 4 discusses the possible stable states and the effect of crease parameters. Finally, Section 5 describes some interesting results.

2 Methodology

We utilize the equivalent bar-and-hinge model to analyze the deformation of the hexagonal origami hypar. The analysis process is simplified to bifurcation branches by group theory. The bifurcation branches can be obtained by symmetry breaking.

2.1 Bar-and-hinge model of non-rigid origami

Bar-and-hinge is a simplified model in finite element analysis of origami [60, 61]. Based on finite element analysis, the total potential energy Π can be expressed as

$$\Pi = U - V \tag{1}$$

where V is the external work and U represents the strain energy. According to the principle of the minimum total potential energy, the finite element equation can be obtained as

$$\mathbf{F} = \mathbf{K}\boldsymbol{\Delta} \tag{2}$$

where $\mathbf{F}$, K, and $\boldsymbol{\Delta}$ donate the force vector, the tangent stiffness matrix, and the generalized displacement vector, respectively. The internal force vector and the tangent stiffness matrix can be assembled from equivalent nodal loads and elementary stiffness matrices.

Compared with rigid origami, the potential energy U of non-rigid origami contains not only folding energy, but also panel deformation energy [36].

$$U = U_F + U_S + U_B \tag{3}$$

where U_F, U_S, and U_B represent crease folding energy, bar stretching energy, and facet bending or

twisting energy, respectively. Then, the tangent stiffness matrix can be expressed by finding displacement variations of Eq. (3) twice [36].

$$\mathbf{K} = \mathbf{K}_F + \mathbf{K}_S + \mathbf{K}_B = \mathbf{K}_{spr} + \mathbf{K}_{bar} \tag{4}$$

where the stiffness of rotational spring elements $\mathbf{K}_{spr}$ only affects folding stiffness of the crease, $\mathbf{K}_F$, and the stiffness of bar elements $\mathbf{K}_{bar}$ contains in-plane stretching and shearing stiffness of the bar $\mathbf{K}_S$ and out-plane bending stiffness of the facet $\mathbf{K}_B$. Thus, elementary stiffness of bar elements and rotational spring elements needs to be solved. The hyperplastic model is selected to simulate the constitutive relationship of bar elements [60, 61]. The elementary stiffness matrices are obtained by

$$\begin{cases} \mathbf{K}_{\mathbf{spr}}^{\mathbf{e}} = \mathbf{K}_{\mathbf{F}}^{\mathbf{e}} = \partial^2 U_F^e / \partial \mathbf{u}^2 = k_{spr}^e \, d\theta / d\mathbf{u} \otimes d\theta / d\mathbf{u} + M_F \, d^2\theta / d\mathbf{u}^2 \\ \mathbf{K}_{\mathbf{B}}^{\mathbf{e}} = \partial^2 U_B^e / \partial \mathbf{u}^2 = k_B^e \, d\theta / d\mathbf{u} \otimes d\theta / d\mathbf{u} + M_B \, d^2\theta / d\mathbf{u}^2 \\ \mathbf{K}_{\mathbf{S}}^{\mathbf{e}} = \partial^2 U_S^e / \partial \mathbf{u}^2 = k_S^e \left(\mathbf{B}_1^T + \mathbf{B}_2 \mathbf{u} \right) \left(\mathbf{B}_1^T + \mathbf{B}_2 \mathbf{u} \right)^T + f_s \mathbf{B}_2 \end{cases} \tag{5}$$

During the simulation of the kinematic path, the tangent stiffness matrix near the bifurcations will be severely ill-conditioned. It can be effectively avoided through group theory [62, 63].

2.2 A group-theoretic approach to the global bifurcation analysis

The essence of the global bifurcation analysis is to solve the vector equilibrium equation

$$\mathbf{f}(\mathbf{u}, \lambda) = \mathbf{0} \tag{6}$$

where $\mathbf{u}$ belongs to an N-dimensional real vector space and λ is a real number. Then, using the symmetry-adapted coordinate system, the Newton-Rapson procedure is implemented by the block-diagonalization,

$$\begin{bmatrix} \mathbf{K}_{v^{(1)}} & 0 & \cdots & 0 \\ 0 & \mathbf{K}_{v^{(2)}} & \cdots & 0 \\ \vdots & \vdots & \cdots & \vdots \\ 0 & 0 & \cdots & \mathbf{K}_{v^{(p)}} \end{bmatrix} \begin{bmatrix} \Delta\mathbf{u}^{(1)} \\ \Delta\mathbf{u}^{(2)} \\ \vdots \\ \Delta\mathbf{u}^{(p)} \end{bmatrix} = \begin{bmatrix} -\mathbf{f}_\lambda \\ 0 \\ \vdots \\ 0 \end{bmatrix} \tag{7}$$

where $\mathbf{K}$ represents the tangent stiffness matrix $\mathbf{K} = \mathrm{d}\mathbf{f} / \mathrm{d}\mathbf{u}$. Decomposed by many block matrices, the original problem can be neatly reduced to a series of independent problems involved with specific

symmetry subspaces.

$$\mathbf{K}_{V^{(1)}}\Delta\mathbf{u}^{(1)} = -\mathbf{f}_{\lambda} \tag{8}$$

In other words, the solution of Eq. (6) can be obtained by solving Eq. (8) associated with different subspaces. For a symmetric structure, its symmetry subgroups are associated with different symmetry subspaces. Therefore, bifurcation branches of the original structure will consist of the bifurcation branches of the corresponding symmetry subgroups [64].

2.3 Symmetry breaking behavior

The transformation from the primary path to bifurcation paths of deployable structures is often accompanied by symmetry breaking behavior [58, 59]. In other words, different bifurcation paths can be obtained by reducing the symmetry order of structures.

The C_{nv} symmetry group contains a total of $2n$ independent symmetry operations [65].

$$C_{nv} = \left\{ C_n^j, \sigma_j \mid j = 1, 2, \cdots, n \right\} \tag{9}$$

where the rotation C_n^j represents that the original structure rotates an angle $2\pi j/n$ around the symmetry axis, $j \in [1, n]$, and σ_j donates the jth reflection along the vertical symmetry plane. Among these symmetry operations, the one-dimensional and two-dimensional irreducible representations are selected to describe the partial symmetry of the original structure, respectively. The irreducible representations are listed as

$$n = \text{even} \begin{cases} \Gamma^{(1)} = A_1, \Gamma^{(2)} = A_2, \Gamma^{(3)} = B_1, \Gamma^{(4)} = B_2 & \text{one-dimensional} \\ \Gamma^{(5)} = E_1, \cdots, \Gamma^{(3+0.5n)} = E_{0.5n-1} & \text{two-dimensional} \end{cases} \tag{10}$$

$$n = \text{odd} \begin{cases} \Gamma^{(1)} = A_1, \Gamma^{(2)} = A_2 & \text{one-dimensional} \\ \Gamma^{(3)} = E_1, \cdots, \Gamma^{(1.5+0.5n)} = E_{0.5n-0.5} & \text{two-dimensional} \end{cases} \tag{11}$$

where $\Gamma^{(i)}$ donates an irreducible representation of the structure, and A_1, $\cdots$, B_1, $\cdots$, E_1, $\cdots$ are basic symmetry representations, respectively. The number of one-dimensional irreducible representations of

C_{nv} is $2\alpha+2$, whereas that of two-dimensional irreducible representations is $(n-1-\alpha)/2$ [66]. The value α equals 0 (or 1) when n is odd (or even). The first item of them indicates the highest-order symmetry, and the final item indicates the lowest-order symmetry. Then, the subgroups can be obtained from these irreducible representations.

$$C_1,\cdots,C_i,\cdots,C_m,C_n,C_v,\cdots,C_{iv},\cdots,C_{mv}\subset C_{nv} \tag{12}$$

where m represents the maximum proper divisor of n, and i includes all the proper divisors of n. Then, the affiliation and symmetry order of these subgroups of C_{nv} can be judged. For instance, C_1 is the lowest-order symmetry group.

A kinematically indeterminate structure is mobile if the symmetry order of internal mechanism mode is higher than that of the self-stress state [57]. In other words, the symmetry order of the self-stress state has to be reduced to ensure the foldability. If the symmetry order of mechanism mode fails to satisfy the full symmetry, the structure will transform into a bifurcation branch with lower-order symmetry. The bifurcation branch matches the symmetry order of the associated constraint modes. That is, we can effectively program the symmetry order of the structure by controlling the constraint mode.

3 Multi-stability of hexagonal origami hypar with six vertices

Figure 1 shows crease patterns of the hexagonal origami hypar. The blue dotted lines and red solid lines represent the valley and mountain creases, respectively. The solid black dots represent z-direction constraints. The geometric and material parameters of the initial pattern are defined similarly to the configuration of the square origami hypar [37]. The fold spacing d and inner fold spacing D are $d = D = 8$mm. The number of the crease layers is $n = 8$. The thickness t is 127 μm . The elastic modulus E for the material is 5GPa, and the Poisson's ratio μ is 0.35. In contrast to the square origami hypar, there are more possibilities for 3D geometry of the hexagonal origami hypar. In this section, we will

investigate multi-stability of the hexagonal origami hypar by studying its stable states with different symmetry orders.

The initial plane pattern of hexagonal origami hypar belongs to C_{6v} symmetry group. To allow the structure to be foldable, the symmetry order of the self-stress state is required to be decreased less than that of the initial pattern [57, 58]. The subgroups of C_{6v} group can be computed by

$$C_1, C_2, C_3, C_4, C_5, C_6, C_v, C_{2v}, C_{3v} \subset C_{6v} \tag{13}$$

According to theorems for assigning mountain and valley creases [67], creases distribution in the preliminary patterns must be symmetric along the diagonals. In other words, the initial pattern cannot transform into a symmetry subgroup containing only cyclic rotations, including C_6, C_3, C_2, and C_1. Namely, we only need to study the cases with mirror symmetry, containing C_{3v}, C_{2v}, and C_v.

According to Section 2, a specific symmetry breaking of the structure is achieved by adjusting the symmetry order of the constraint mode. Figure 1(a) shows the three-dimensional axonometric view of the pattern, and Figures 1(b), (c) and (d) show different constraint modes leading to origami configurations with different symmetry groups. The mountain and valley properties of the innermost creases will change with different symmetry. Figures 1(b), (c), and (d) corresponds to C_{3v}, C_{2v}, and C_v symmetry, respectively.

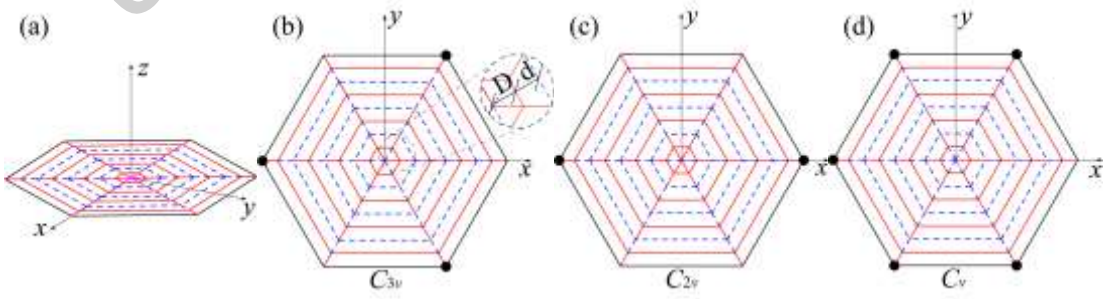

Figure 1 Crease patterns of the hexagonal origami hypar. (a) Three-dimensional perspective of plane pattern (b) to (e) Different constraint modes and patterns corresponding to C_{3v}, C_{2v}, and C_v symmetry.

3.1 Hexagonal origami hypar with C_{3v} symmetry

Among the subgroups, the highest symmetric mechanism mode is C_{3v} symmetry. The initial 3D configuration can be obtained by loading the equivalent bar-and-hinge model in *z*-direction. The applied forces to fold the initial pattern are adjusted based on the folding of the square origami hypar [37]. The loading in *z*-direction we used is shown in Figure 2(a). Then, we get the initial 3D configuration, see Figure 2(b), by MERLN2_v1.1 with the constraint and the applied forces in Figure 2(a). However, it is a random state instead of a stable state. When the system is released from the external loads, it will recover into one of its stable states, as shown in Figure 2(c).

In order to find other stable states with C_{3v} symmetry, we further analyze the stable 3D configurations by the bar-and-hinge model. In Figure 3(a), three lower outermost vertices are constrained, whereas downward displacements are applied on the remaining three vertices. Because of the increasing of the displacements, the structure first unfolds from the first stable state (state 1) to an approximately fully flat state (state 2). Then, it refolds along the creases to a new equilibrium (state 3). The total potential energy reaches another minimum at state 3, as shown in Figure 3(e). According to the energy principle, the new equilibrium is the second stable state of the hexagonal origami hypar with C_{3v} symmetry.

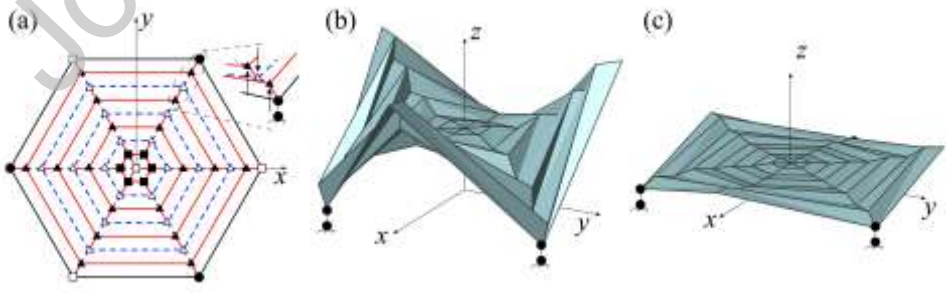

Figure 2 3D origami configuration with C_{3v} symmetry. (a) Applied forces in z-direction (hollow circle ○ represents downward force F_0, solid square ■ represents upward force $2.25F_0$, hollow triangle △ represents downward force $4F_0$, solid triangle ▲ represents upward force $4F_0$, hollow square □

represents upward force $2F_0$, solid circle ● represents constraints in z-direction) (b) Initial 3D geometry configuration. (c) 3D configuration in a stable state.

The stored energy-displacement relation precisely reflects the bistability of the structure. In Figure 3(e), the total potential energy E_T contains the tensile and shear energy E_s, the bending energy E_B, and the folding energy E_F. During the transition from stable state 1 to stable state 3, E_F increases with the decrease of the folding angle and accounts for the largest proportion of E_T. This property indicates that this structure folds preferentially at the creases. Panel deformation energy $E_B + E_S$ accounts for a certain proportion of the total potential energy, especially when the structure is close to stable states. Thus, in terms of folding energy, the panel deformation energy cannot be ignored. Namely, the hexagonal origami hypar is a non-rigid origami structure. In other words, the panel deformations need to be considered during folding.

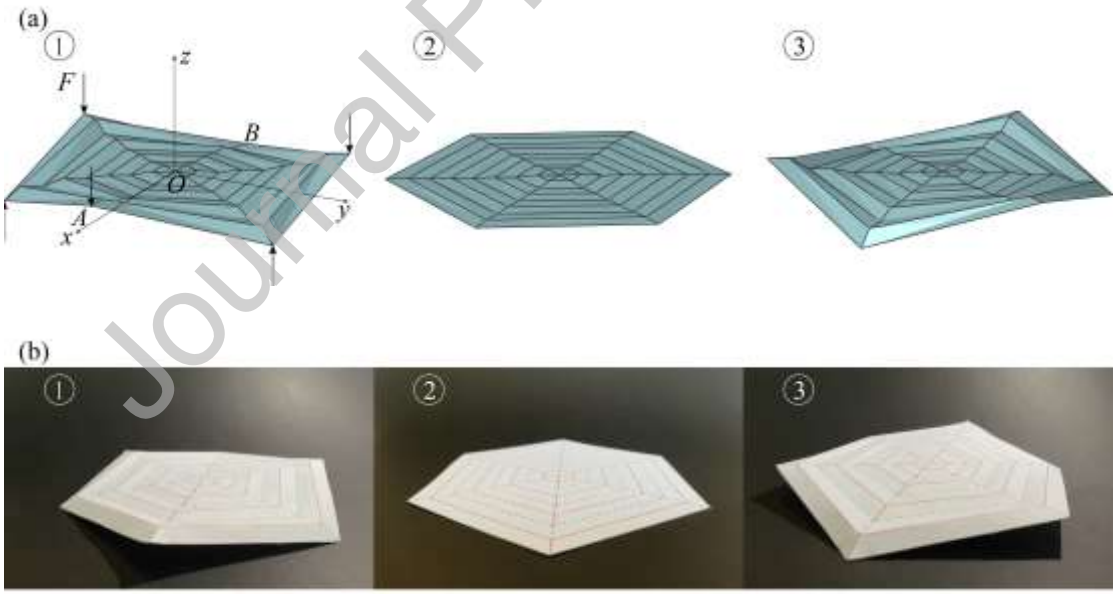

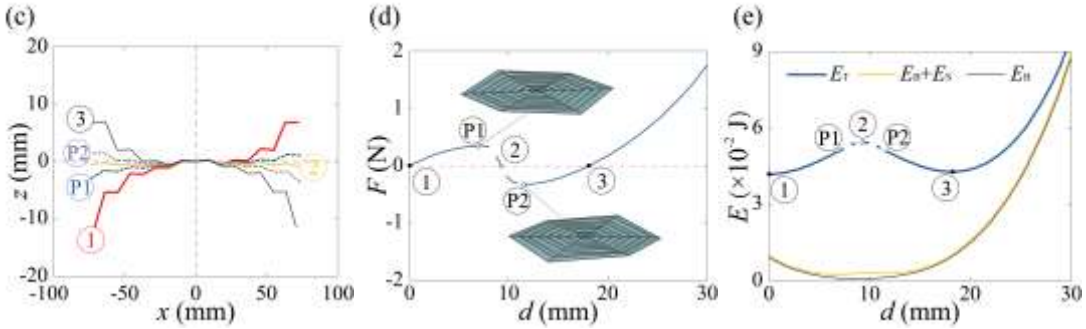

Figure 3 Multi-stability of hexagonal origami hypar with C_{3v} symmetry. (a) Key states among the whole process. (b) Physical models. (c) Changing profile of the set of diagonal creases on *x*-axis (i.e., diagonal AOB). (d) Equilibrium load versus displacement curves of single load point. (e) Stored energy versus displacement curves.

As for the specific composition of the deformation energy, E_S increases while E_B decreases with the flattening of the panels. E_B accounts for the most of the panel deformation energy around the stable states while E_S accounts for the most of the panel deformation energy near the fully expanded state. That is, the deformation of the panels is dominated by the bending near the stable states and by the tension, compression and shear near the fully expanded state. Moreover, E_B changed obviously during the whole process while E_S only changed obviously near the fully flattened state. Namely, the bending deformation of the panels exists in the whole process while the tensile deformation of the panels only exists near the fully flattened state. In addition, the proportion of E_S in E_T is still small even near the fully expanded state, whereas the proportion of E_B in E_T is large near the stable states. That is, the panel deformation of the hexagonal origami hypar is mainly controlled by the bending deformation.

The equilibrium load-displacement curves further verify these two stable states. In Figure 3(d), these two stable states correspond exactly to the two zero points that cross reference line $F = 0$ in the positive direction. State P1 and state P2 both reach the peak value of the equilibrium load during folding. Moreover, according to Figure 3(d), they are roughly symmetric about the center point corresponding

to state 2. Similarly, the two stable states (i.e., state 1 and state 3) are symmetric about state 2 as the center point. Figure 3(c) reflects the changing profile of the $y = 0$ section during folding. The two stable states (i.e., state 1 and state 3) and the two peak force states (i.e., state P1 and state P2) are mirror along $x = 0$, respectively. The intermediate state 2 is mirror symmetric about the x-axis, but not fully flattened. Moreover, except for the innermost folds, the mountain and valley properties of the creases remain constant during the transition between the two stable states.

3.2 Hexagonal origami hypar with C_{2v} symmetry

The first stable state with C_{2v} symmetry is obtained by the same method at the beginning of Section 3.1. The difference is that this situation requires the origami pattern and constraints shown in Figure 1(b). The unconstrained outermost vertices are all load points since the constraint conditions have changed. The load size and direction of the new load points are same as the load size and direction represented by the white square in Figure 2(a). The loading conditions for the remaining nodes are the same as those shown in Figure 2(a).

Then, we further analyze the stable 3D configurations with C_{2v} symmetry by the similar method as Section 3.1. The two outermost vertices on an adjacent diagonal are constrained, and upward loads are applied on the remaining four outermost vertices on two adjacent diagonals. Then, two lower outermost vertices are constrained, whereas the downward displacements are applied on the remaining four outermost vertices, as shown in Figure 4(a1). As the increasing of the displacements, the structure first unfolds from the initial stable state 1 to approximately fully flattened state 2. Then, it refolds along the creases to a new equilibrium state 3. The total potential energy at state 3 reaches another minimum, as shown in Figure 4(e). According to the energy principle, the new equilibrium is the second stable state of the hexagonal origami hypar with C_{2v} symmetry.

Same as the hexagonal origami hypar with C_{3v} symmetry, in Figure 4(e), the bistability of the hexagonal origami hypar with C_{2v} symmetry can be directly reflected by the stored energy versus displacement curves. According to Figure 4(e), the hexagonal origami hypar with C_{2v} symmetry is non-rigid, and the panel deformation of the hexagonal origami hypar is mainly controlled by the bending deformation. Moreover, the variation tendencies of equilibrium load and potential energy during the transition between the two stable states reflected in Figure 4(d) and 4(e) are similar to those shown in Figure 3(d) and 3(e), respectively. Figure 4(c) reflects the same mountain and valley properties of the creases and symmetry between corresponding states during the whole process. Contrast with the hexagonal origami hypar with C_{3v} symmetry, the key states during the whole transition with C_{2v} symmetry are all mirror symmetric about $x = 0$.

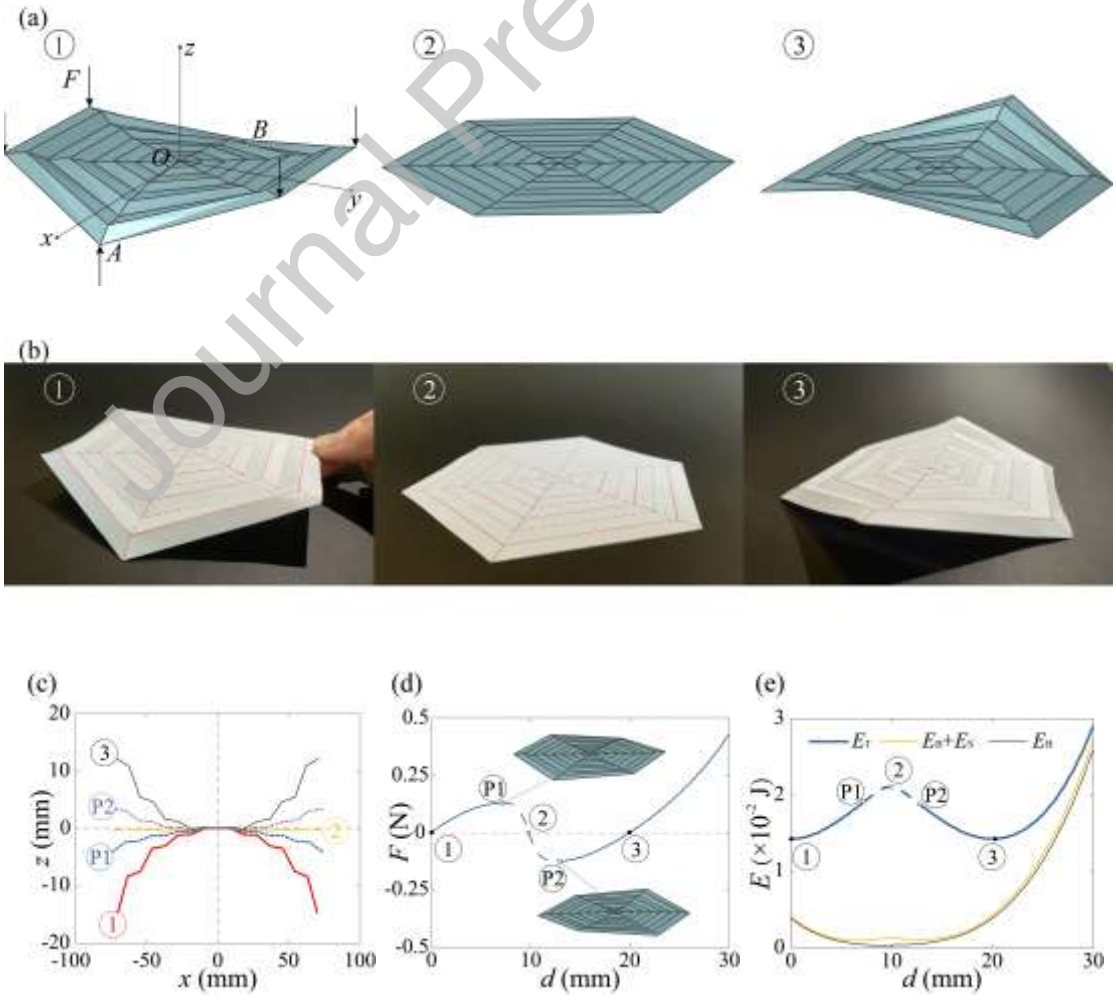

Figure 4 Multi-stability of hexagonal origami hypar with C_{2v} symmetry. (a) Key states among the whole process. (b) Physical model. (c) Changing profile of the set of diagonal creases on *x*-axis (i.e., diagonal AOB). (d) Equilibrium load versus displacement curves of a single load point. (e) Stored energy versus displacement curves.

3.3 Hexagonal origami hypar with C_v symmetry

The 3D configuration with C_v symmetry can be achieved by further reducing the symmetry order. The first stable state with C_v symmetry is obtained by the same method in Section 3.1. The difference is that this situation requires the origami pattern and constraints shown in Figure 1(c). The only outermost free vertex is subjected to an upward load of $3F_0$ in *z*-direction. The loading conditions for the remaining nodes are the same as those shown in Figure 2(a).

Then, we further analyze the stable 3D configurations with C_v symmetry. The five outermost vertices are constrained, and downward loads are applied on the remaining outermost vertex. Then, the five higher outermost vertices are constrained and an upward displacement is applied to the remaining vertex, as shown in Figure 5(a1). As the increasing of the displacement, the structure first unfolds from the first stable state 1 to approximately fully flattened state 2. Then, it refolds along the creases to a new equilibrium state 3. The total potential energy reaches another minimum at state 3, as shown in Figure 5(e). According to the energy principle, the new equilibrium is the second stable state of the hexagonal origami hypar with C_v symmetry.

Similar to the above two cases, the bistability of the hexagonal origami hypar with C_v symmetry can be directly reflected by Figure 5(e). The hexagonal origami hypar with C_v symmetry is a non-rigid origami structure and the panel deformation of the hexagonal origami hypar is mainly controlled by the bending deformation. Moreover, Figure 5(d) and Figure 5(e) reflect similar variation tendencies of

equilibrium load and potential energy as those of the other bifurcation paths. Figure 5(c) reflects the same mountain and valley properties of the creases and symmetry between corresponding states during the whole process with Figure 3(c) and Figure 4(c). Compared with the hexagonal origami hypar with C_{3v} symmetry and C_{2v} symmetry, the key states among the whole process show no symmetry in $y = 0$ section.

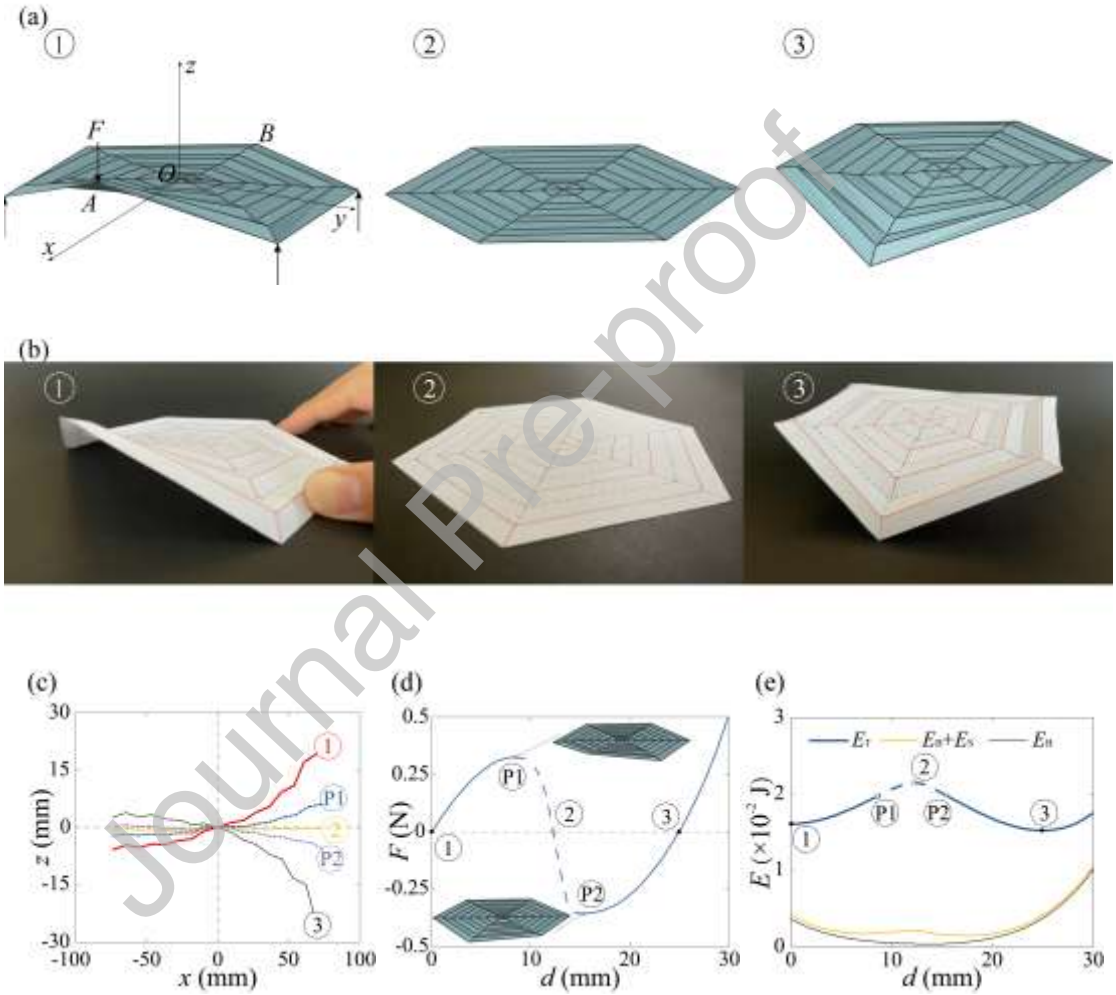

Figure 5 Multi-stability of hexagonal origami hypar with C_v symmetry. (a) Key states among the whole process. (b) Physical model. (c) Changing profile of the set of diagonal creases on x-axis (i.e., diagonal AOB). (d) Equilibrium load versus displacement curves of a single load point. (e) Stored energy versus displacement curves.

In summary, the bistability of hexagonal origami hypar in each bifurcation branch is same as the square

origami hypar [29]. There are two stable states along each bifurcation branch. They are approximately symmetric along the horizontal plane. The mountain and valley properties of the creases remain unchanged between these two stable states.

4 Discussion

In this section, we discuss the differences and transition among these three bifurcation branches. Several metrics are chosen to represent the energy barrier of multistable transitions in Section 4.1, and some relevant influencing factors are studied in Section 4.2.

4.1 Multi-stability of hexagonal origami hypar with different symmetries

To compare different bifurcation branches, we put them into a unified coordinate system for discussion, as shown in Figure 6. The points $\mathrm{I_a}$, $\mathrm{P1_a}$, $\mathrm{P2_a}$, $\mathrm{III_a}$, points $\mathrm{I_b}$, $\mathrm{P1_b}$, $\mathrm{P2_b}$, $\mathrm{III_b}$, and points $\mathrm{I_c}$, $\mathrm{P1_c}$, $\mathrm{P2_c}$, $\mathrm{III_c}$ correspond to the key states 1, P1, P2, and 3 on the bifurcation branches with C_v, C_{2v} and C_{3v} symmetry described in Section 3, respectively. To ensure the fairness of the comparison among the various numbers of loading points for different bifurcation branches, the total equilibrium load is chosen as the *y*-axis. In Section 3, we have obtained the equilibrium load curves at a single loading point for each bifurcation branch. Therefore, the total equilibrium load should be the sum of the equilibrium loads at all loading points in each branch. Then, based on the symmetry of each bifurcation branch, the equilibrium loads of all loading points are identical. That is, we can obtain the total equilibrium load by multiplying the equilibrium load at a single load point by the number of loading points. For the bifurcation branch with C_{3v} symmetry, we applied downward displacements on the three free outmost vertices. Thus, total equilibrium load bifurcation branch with C_{3v} symmetry equals to the equilibrium load at a single loading point multiplied by three. For the bifurcation branch with C_{2v} symmetry, there are four loading points. Therefore, its total equilibrium load equals to the

equilibrium load at a single loading point multiplied by four. For the bifurcation branch with C_v symmetry, we only applied upward displacement on one vertex. Thus, the total equilibrium load of bifurcation branch with C_v symmetry equals to the equilibrium load at a single loading point itself.

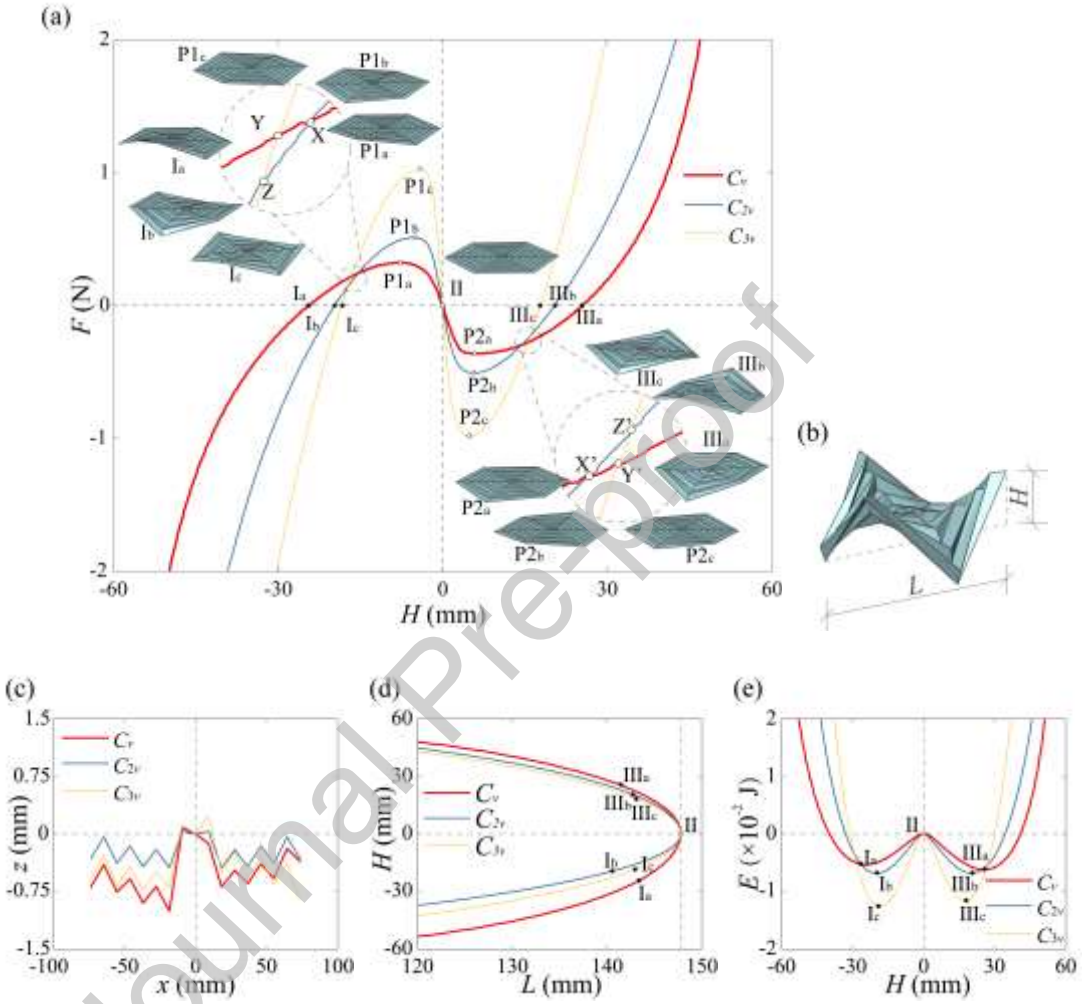

Figure 6 Comparison of various bifurcation branches. (a) Total equilibrium load-displacement curves of three bifurcation branches. (b) Physical meaning of span (L) and height (H). (c) Profile of the y = 0 section in state 2. (d) Span versus height curves. (e) Total energy versus height curves.

According to Figure 6(a), seven possible critical points can be found in total, including point X, Y, Z, X', Y', Z', and II. Figure 6(c) shows the profiles of the y = 0 section of the structure in each bifurcation branches at state 2. Since the displacements are calculated by finite element analysis, the state 2 shown in Figure 6(c) is an approximate solution. However, it can be judged from the folding tendency that the

hexagonal origami hypar is fully expanded in state 2 as point II in Figure 6(d). Namely, point II is one of the critical points of these three bifurcation branches. As for the other possible critical points, the states corresponding to various bifurcation branches at the intersections are different. In Figure 6(d), these three bifurcation branches have no intersection except point II. Namely, point II is the only critical point of these three bifurcation branches.

Then, we select the state corresponding to the critical point II as the zero potential energy state. Figure 6(e) reflects the total energy (E_T) variation of the hexagonal origami hypar from stable state 1 to stable state 3, respectively. Critical point II represents the fully flattened state in the three bifurcation branches. The energy barrier of conversion among these stable states can be reflected by the difference between extreme value of stored energy curves. Compared with the stable states with C_{2v} and C_v symmetry, unfolding from the stable state with C_{3v} symmetry to the fully unfolded state is the most difficult to achieve. Unfolding from the stable states with C_{2v} symmetry is easier, and unfolding from the stable states with C_v symmetry is the easiest.

In summary, around this thickness, the stable states with C_{3v} symmetry has the most significant energy barrier to transform to the other stable states, followed by the stable states with C_{2v} symmetry, and the stable states with C_v symmetry has the slightest energy barrier.

4.2 Influence of geometric parameters

To obtain more general conclusions, we also discuss the effects of different parameters on the stable states of the hexagonal origami hypar, including the thickness of material t and the fold spacing d. Different numerical examples are summarized in Table 1.

Table 1 Parameters of numerical examples.

Model	T0	T1	T2	T3	T4	F1	F2	F3	F4	F5
L (mm)	64	64	64	64	64	60	60	60	60	60
D (mm)	8	8	8	8	8	12	12	12	12	12

d (mm)	8	8	8	8	8	4	6	8	12	16
t (μm)	127	40	76	200	240	127	127	127	127	127

4.2.1 Influence of material thickness

The rest of the parameters, including d, D, and n, are the same as the reference model, as Model T0 to T4 shown in Table 1.**Error! Reference source not found.**Then, we utilize the same method to simulate the multi-stability of the Model T1 to T4. Figure 7(a), (c), and (e) show the results correspond to C_{3v}, C_{2v}, and C_v symmetry, respectively. The point $\mathrm{T0_I}$ represents the stable state 1 in Model T0, and the point $\mathrm{T0_{III}}$ represents the stable state 3 in Model T0.

Figure 7(a), (c), and (e) show that the peak values of the equilibrium load increase with the material thickness during the transitions of two stable states. The absolute value of F indicates its structural height, and the positive or negative of F indicates whether it increases along the positive z-axis. If F increases along the positive z-axis, it is negative. Otherwise, F is positive. To make the results clearer, we have extracted the peaks of the balanced load and marked them in Figure 7(b), (d), and (f). The equilibrium load versus height curves during the transition between two stable states consist of two peaks, and the tendencies of them are centrosymmetric along the origin point. The whole process can be divided into two phases with the origin point as the cut-off point. The first phase, called loading phase, is the change from stable state 1 to a fully flatted state under external loads. Similarly, the second phase, called recovery phase, is the change from the fully flatted state to the other stable state 3. The peak equilibrium load in the loading phase is F_L, and the peak equilibrium load in the recovery phase is F_R. Figure 7(b), (d), (f) show that F_L and F_R are proportional to the third power of the material thickness (i.e., t^3). The fitting plots f_L and f_R in the Figure 7(b), (d), and (f) are obtained by linear fitting with t^3 as the independent variable through the MATLAB toolbox.

In the simulation process, the stiffness of the creases and the bending stiffness of the panels are related

to t^3 while the tension-compression stiffness of the panels is related to t [60]. Then, we can further verify the similar results in Section 3 that the folding of the structure is mainly realized by the folding of the creases and the bending of the panels, and the tension and compression deformation of the panels only accounts for a small part.

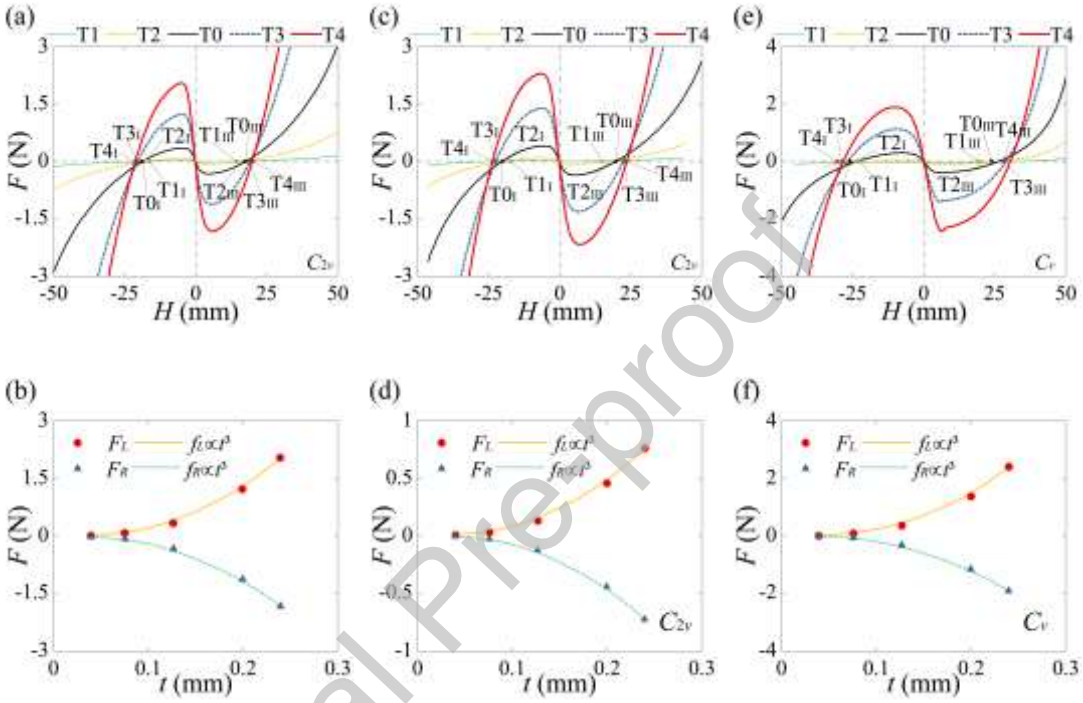

Figure 7 Effects of material thickness. (a), (c), and (e) Equilibrium load versus height curves of a single load point. (b), (d), and (f) Relationship between the material thickness (t) and the peak equilibrium load (F).

As for the height of the structure, we refer to the height at which the structure reaches a stable state as the stable height H. Figure 7(a), (c), and (e) show that the stable height increases with material thickness. Same as the peak equilibrium load, each equilibrium load-height curve has two stable heights corresponding to the two stable states. The stable height corresponding to stable state 1 is called H_{I} and the stable height corresponding to stable state 3 is called H_{III}. The absolute value of H is its height and the plus or minus sign indicates whether H increases along the positive z-axis. If H increases

along the positive *z*-axis, it is positive. Otherwise, *H* is negative. Thus, for the equilibrium load versus height curve, the farther the stable state from $H = 0$, the higher the stable height will be.

In summary, the peak equilibrium loads and the stable heights with same symmetry, all increase with material thickness. In particular, the magnitude of the peak equilibrium load is positively related to the third power of the material thickness.

4.2.2 Influence of crease length

We adjust the geometric parameters of the reference model to the variation of the *d* while keeping the *L* constant. The *n* varies with the *d* as Model F1 to F5 shown in Table 1. The outer most creases are kept peak and the various patterns are shown in Figure 8. Then, the bistability of the Model F1 to Model F5 can be simulated by the same method. Figure 9(a) to (c) show the results correspond to C_{3v}, C_{2v}, and C_v symmetry, respectively. The point $F1_{P1}$ represents the state P1 in Model F1, and the point $F1_{P2}$ represents the state P2 in Model F1.

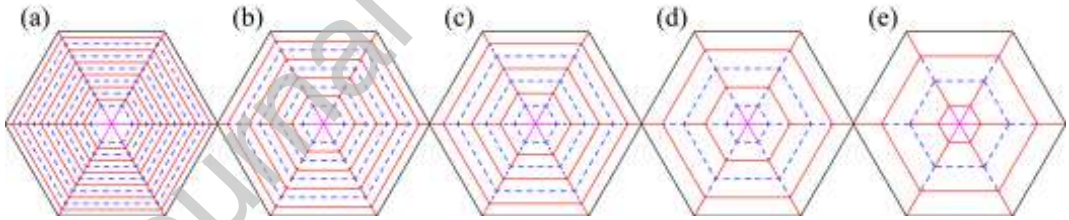

Figure 8 Crease patterns with different *d*. (a) to (e) correspond to Model F1 to Model F5, respectively.

In Figure 9, the peak equilibrium loads increase with the spacing *d* during the transitions of two stable states with the same symmetry. Since *L* does not change, the change of *d* will directly lead to the change of *n*. For simplicity, we unify these two variables as the total length of all creases, called crease length (denoted by l). The relationships between the crease length and the peak equilibrium loads are shown in Figure 9(d). For the three different symmetry cases, the peak equilibrium loads in both the loading and recovery phases increase with crease length. In other words, the hexagonal origami hypar

with longer crease lengths is more difficult to be folded. As for the stable height, it is related to the crease spacing, crease layer number and crease length. The specific law of their influence needs to be further studied.

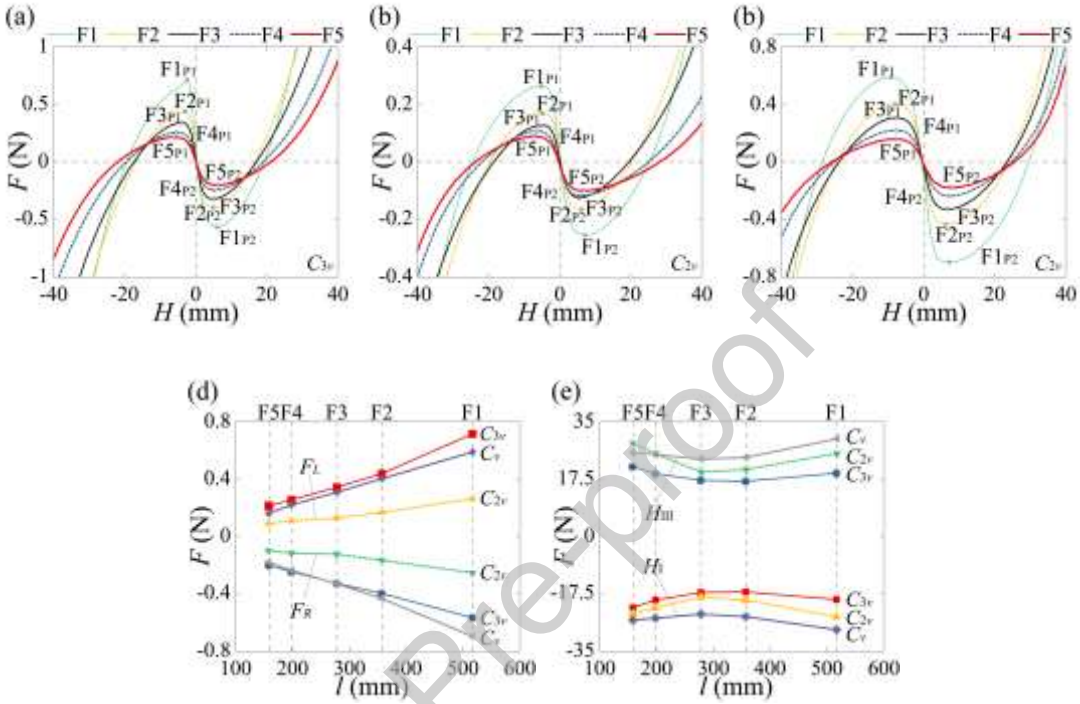

Figure 9 Effect of crease spacing. (a) to (c) Equilibrium load versus height curves of a single load point. (d) Relationship between the creases length *l* and the peak equilibrium loads F_L and F_R. (e) Relationship between the creases length *l* and the stable heights H_{I} and H_{III}.

In summary, the magnitude values of peak balanced loads increase with the crease length. In other words, stable states of hexagonal origami hypar with longer crease length has more significant energy barrier. Admittedly, the effects of different spans *L* and number of initial polygon sides on the stable states of hexagonal origami hypar can be further studied for various sizes. The obtained data can be analyzed by deep learning [68] to get much more precise numerical influence. These conclusions could provide support for the programmable design of metamaterials [69, 70] based on hexagonal origami hypar.

5 Conclusions

In this work, we have adopted bar-and-hinge model, a group-theoretic approach, and symmetry breaking for exploring the multi-stability of hexagonal origami hypar. The bar-and-hinge model is applied to simulate the whole folding and unfolding process. Concurrently, the group-theoretic approach is selected to avoid singularity in the stiffness matrix near the bifurcations. The symmetry subgroups obtained by symmetry breaking are introduced to trace the corresponding bifurcation branches. The multi-stability of the structure can be obtained by analyzing multi-stability of all the bifurcation branches, respectively.

1) Hexagonal origami hypar is always non-rigid during folding. The non-rigid deformation is mainly realized by the bending deformation of each panel.

2) Hexagonal origami hypar has three distinct types bifurcation paths, including C_{3v}, C_{2v}, and C_v symmetry. All bifurcation branches exhibit bistability. Thus, the hexagonal origami hypar has six independent stable states.

3) These stable states can be converted to each other only through the fully flattened state. The initial state with the most significant energy barrier is the stable states with C_{3v} symmetry, and the slightest one is the stable states with C_v symmetry. The energy barrier increases with the material thickness or crease length.

Further, our method can be extended for multi-stability analysis of origami structures with higher-order symmetry. It would systematically describe the transition between their stable states by simplifying the original folding analysis into the collection of multi-stability in different bifurcation branches.

Yao Chen: Methodology, Resources, Formal analysis, Validation, Investigation, Writing - original draft, Writing - review & editing, Supervision, Project

administration, Funding acquisition. **Ruizhi Xu**: Conceptualization, Investigation, Data curation, Formal analysis, Validation, Methodology, Software, Writing - original draft. **Chenhao Lu:** Formal analysis, Software, Writing - review & editing. **Ke Liu:** Supervision, Methodology, Validation, Writing - review & editing. **Jian Feng:** Supervision, Validation, Writing - review & editing. **Pooya Sareh:** Supervision, Validation, Writing - review & editing, Funding acquisition.

Declaration of interests

☒ The authors declare that they have no known competing financial interests or personal relationships that could have appeared to influence the work reported in this paper.

Acknowledgement

This work was supported by the National Natural Science Foundation of China (Grants No. 51978150 and 52050410334), Southeast University "Zhongying Young Scholars" project, and the Fundamental Research Funds for the Central Universities. KL acknowledges the support by Peking University, College of Engineering. The authors are grateful to the editors and anonymous reviewers for their professional comments and valuable suggestions in improving the quality of the paper.

Data availability

Data will be made available on request.

References

[1] E. Siefert, E. Reyssat, J. Bico, B. Roman, Bio-inspired pneumatic shape-morphing elastomers. Nature Materials. 18 (1) (2019) 24-28. https://doi.org/10.1038/s41563-018-0219-x

[2] C. Huang, T. Tan, X. Hu, F. Yang, Z. Yan, Bio-inspired programmable multi-stable origami. Applied Physics Letters. 121 (5) (2022) 51902. https://doi.org/10.1063/5.0088242

[3] Z. Li, Q. Yang, R. Fang, W. Chen, H. Hao, Origami metamaterial with two-stage programmable compressive strength under quasi-static loading. International Journal of Mechanical Sciences. 189 (2021) 105987. https://doi.org/10.1016/j.ijmecsci.2020.105987

[4] Z. Meng, W. Chen, T. Mei, Y. Lai, Y. Li, C.Q. Chen, Bistability-based foldable origami mechanical logic gates. Extreme Mechanics Letters. 43 (2021) 101180. https://doi.org/10.1016/j.eml.2021.101180

[5] S. Yi, L. Wang, Z. Chen, J. Wang, X. Song, P. Liu, Y. Zhang, Q. Luo, L. Peng, Z. Wu, C.F. Guo, L. Jiang, High-throughput fabrication of soft magneto-origami machines. Nature Communications. 13 (1) (2022). https://doi.org/10.1038/s41467-022-31900-5

[6] J. Kaufmann, P. Bhovad, S. Li, Harnessing the multistability of kresling origami for reconfigurable articulation in soft robotic arms. Soft Robotics. 9 (2) (2022) 212-223. https://doi.org/10.1089/soro.2020.0075

[7] M. Mirkhalaf, F. Barthelat, Design, 3D printing and testing of architectured materials with bistable interlocks. Extreme Mechanics Letters. 11 (2017) 1-7. https://doi.org/10.1016/j.eml.2016.11.005

[8] H. Qiu, Y. Feng, Y. Gao, S. Zeng, J. Tan, The origami inspired design of polyhedral cells of truss core panel. Thin-Walled Structures. 163 (2021) 107725. https://doi.org/10.1016/j.tws.2021.107725

[9] Y. Zhang, Q. Wang, M. Tichem, F. van Keulen, Design and characterization of multi-stable mechanical metastructures with level and tilted stable configurations. Extreme Mechanics Letters.

34 (2020) 100593. https://doi.org/10.1016/j.eml.2019.100593

[10] H. Yasuda, T. Tachi, M. Lee, J. Yang, Origami-based tunable truss structures for non-volatile mechanical memory operation. Nature Communications. 8 (1) (2017) 962. https://doi.org/10.1038/s41467-017-00670-w

[11] P. Bhovad, J. Kaufmann, S. Li, Peristaltic locomotion without digital controllers: exploiting multi-stability in origami to coordinate robotic motion. Extreme Mechanics Letters. 32 (2019) 100552. https://doi.org/10.1016/j.eml.2019.100552

[12] L.S. Novelino, Q. Ze, S. Wu, G.H. Paulino, R. Zhao, Untethered control of functional origami microrobots with distributed actuation. Proceedings of the National Academy of Sciences. 117 (39) (2020) 24096-24101. https://doi.org/10.1073/pnas.2013292117

[13] Z. Zhai, Y. Wang, H. Jiang, Origami-inspired, on-demand deployable and collapsible mechanical metamaterials with tunable stiffness. Proceedings of the National Academy of Sciences-PNAS. 115 (9) (2018) 2032-2037. 1 https://doi.org/10.1073/pnas.1720171115

[14] X. Zhang, J. Ma, M. Li, Z. You, X. Wang, Y. Luo, K. Ma, Y. Chen, Kirigami-based metastructures with programmable multistability. Proceedings of the National Academy of Sciences. 119 (11) (2022). https://doi.org/10.1073/pnas.2117649119

[15] M. Schenk, S.D. Guest, Geometry of miura-folded metamaterials. Proceeding of the National Academy of Sciences of the United States of America. 110 (9) (2013) 3276-3281. https://doi.org/10.1073/pnas.1217998110

[16] H. Fang, K.W. Wang, S. Li, Asymmetric energy barrier and mechanical diode effect from folding multi-stable stacked-origami. Extreme Mechanics Letters. 17 (2017) 7-15. https://doi.org/10.1016/j.eml.2017.09.008

[17] S. Li, K.W. Wang, Fluidic origami with embedded pressure dependent multi-stability: a plant inspired innovation. Journal of the Royal Society Interface. 12 (111) (2015) 20150639. https://doi.org/10.1098/rsif.2015.0639

[18] H. Yasuda, J. Yang, Reentrant origami-based metamaterials with negative Poisson's ratio and bistability. Physical Review Letters. 114 (18) (2015) 185502. https://doi.org/10.1103/PhysRevLett.114.185502

[19] K. Yamaguchi, H. Yasuda, K. Tsujikawa, T. Kunimine, J. Yang, Graph-theoretic estimation of reconfigurability in origami-based metamaterials. Materials & Design. 213 (2022) 110343. https://doi.org/10.1016/j.matdes.2021.110343

[20] H. Fang, Y. Zhang, K.W. Wang, Origami-based earthworm-like locomotion robots. Bioinspiration & Biomimetics. 12 (6) (2017) 65003. https://doi.org/10.1088/1748-3190/aa8448

[21] H. Han, L. Tang, D. Cao, L. Liu, Modeling and analysis of dynamic characteristics of multi-stable waterbomb origami base. Nonlinear Dynamics. 102 (4) (2020) 2339-2362. https://doi.org/10.1007/s11071-020-06082-8

[22] L. Lu, X. Dang, F. Feng, P. Lv, H. Duan, Conical kresling origami and its applications to curvature and energy programming. Proceedings of the Royal Society A-Mathematical Physical and Engineering Sciences. 478 (2257) (2022) 20210712. https://doi.org/10.1098/rspa.2021.0712

[23] R. Tao, L. Ji, Y. Li, Z. Wan, W. Hu, W. Wu, B. Liao, L. Ma, D. Fang, 4D printed origami metamaterials with tunable compression twist behavior and stress-strain curves. Composites Part B: Engineering. 201 (2020) 108344. https://doi.org/10.1016/j.compositesb.2020.108344

[24] J.L. Silverberg, J. Na, A.A. Evans, B. Liu, T.C. Hull, C.D. Santangelo, R.J. Lang, R.C. Hayward, I. Cohen, Origami structures with a critical transition to bistability arising from hidden degrees of

freedom. Nature Materials. 14 (4) (2015) 389-393. https://doi.org/10.1038/nmat4232

[25] J. Ma, S. Zang, H. Feng, Y. Chen, Z. You, Theoretical characterization of a non-rigid-foldable square-twist origami for property programmability. International Journal of Mechanical Sciences. 189 (2021) 105981. https://doi.org/10.1016/j.ijmecsci.2020.105981

[26] H. Yasuda, K. Johnson, V. Arroyos, K. Yamaguchi, J.R. Raney, J. Yang, Leaf-like origami with bistability for self-adaptive grasping motions. Soft Robotics (2022). https://doi.org/10.1089/soro.2021.0008

[27] S. Kamrava, D. Mousanezhad, H. Ebrahimi, R. Ghosh, A. Vaziri, Origami-based cellular metamaterial with auxetic, bistable, and self-locking properties. Scientific Reports. 7 (1) (2017). https://doi.org/10.1038/srep46046

[28] S. Kamrava, R. Ghosh, Z. Wang, A. Vaziri, Origami-inspired cellular metamaterial with anisotropic multi-stability. Advanced Engineering Materials. 21 (2) (2019) 1800895. https://doi.org/10.1002/adem.201800895

[29] E.T. Filipov, M. Redoutey, Mechanical characteristics of the bistable origami hypar. Extreme Mechanics Letters. 25 (2018) 16-26. https://doi.org/10.1016/j.eml.2018.10.001

[30] Y. Chen, J. Yan, J. Feng, Geometric and kinematic analyses and novel characteristics of origami-inspired structures. Symmetry. 11 (9) (2019) 1101. https://doi.org/10.3390/sym11091101

[31] H. Feng, R. Peng, S. Zang, J. Ma, Y. Chen, Rigid foldability and mountain-valley crease assignments of square-twist origami pattern. Mechanism and Machine Theory. 152 (2020) 103947. https://doi.org/10.1016/j.mechmachtheory.2020.103947

[32] Huffman, Curvature and creases: a primer on paper. IEEE Transactions on Computers. 25 (10) (1976) 1010-1019. 1 https://doi.org/10.1109/TC.1976.1674542

[33] W. Wu, Z. You, Modelling rigid origami with quaternions and dual quaternions. Proceedings of the Royal Society A: Mathematical, Physical and Engineering Sciences. 466 (2119) (2010) 2155-2174. 10.1098/rspa.2009.0625

[34] K. Hayakawa, M. Ohsaki, Equilibrium path and stability analysis of rigid origami using energy minimization of frame model. Frontiers in Built Environment. 8 (2022) 995710. https://doi.org/10.3389/fbuil.2022.995710

[35] J. Li, Y. Chen, X. Feng, J. Feng, P. Sareh, Computational modeling and energy absorption behavior of thin-walled tubes with the kresling origami pattern. Journal of the International Association for Shell and Spatial Structures. 62 (2) (2021) 71-81. https://doi.org/10.20898/j.iass.2021.008

[36] J. Tao, S. Li, Asymmetric multi-stability from relaxing the rigid-folding conditions in a stacked Miura-ori cellular solid. Thin-Walled Structures. 179 (2022) 109685. https://doi.org/10.1016/j.tws.2022.109685

[37] K. Liu, T. Tachi, G.H. Paulino, Invariant and smooth limit of discrete geometry folded from bistable origami leading to multistable metasurfaces. Nature Communications. 10 (1) (2019) 4238. https://doi.org/10.1038/s41467-019-11935-x

[38] J. Cehula, V. Prusa, Computer modelling of origami-like structures made of light activated shape memory polymers. International Journal of Engineering Science. 150 (2020) 103235. https://doi.org/10.1016/j.ijengsci.2020.103235

[39] Y.C. Hu, Y.X. Zhou, K.W. Kwok, K.Y. Sze, Simulating flexible origami structures by finite element method. International Journal of Mechanics and Materials in Design. 17 (4) (2021) 801-829. https://doi.org/10.1007/s10999-021-09538-w

[40] T. Yuan, L. Tang, Z. Liu, J. Liu, Nonlinear dynamic formulation for flexible origami-based deployable structures considering self-contact and friction. Nonlinear Dynamics. 106 (3) (2021) 1789-1822. https://doi.org/10.1007/s11071-021-06860-y

[41] S.J.P. Callens, A.A. Zadpoor, From flat sheets to curved geometries: origami and kirigami approaches. Materials Today. 21 (3) (2018) 241-264. https://doi.org/10.1016/j.mattod.2017.10.004

[42] E.D. Demaine, M.L. Demaine, V. Hart, G.N. Price, T. Tachi, (Non)existence of pleated folds: how paper folds between creases. Graphs and Combinatorics. 27 (3) (2011) 377-397. https://doi.org/10.1007/s00373-011-1025-2

[43] M.A. Dias, L.H. Dudte, L. Mahadevan, C.D. Santangelo, Geometric mechanics of curved crease origami. Physical Review Letters. 109 (11) (2012) 114301. https://doi.org/10.1103/PhysRevLett.109.114301

[44] M.A. Dias, C.D. Santangelo, The shape and mechanics of curved-fold origami structures. EPL. 100 (5) (2012) 54005. https://doi.org/10.1209/0295-5075/100/54005

[45] A. Liu, M. Johnson, C. Sung, Increasing reliability of self-folding of the origami hypar. Journal of Mechanical and Robotics-transactions of the ASME. 14 (6) (2022) 60904. https://doi.org/10.1115/1.4054310

[46] L. Alese, Propagation of curved folding: the folded annulus with multiple creases exists. Beitrage zur Algebra und Geometrie-contributions to Algebra and Geometry. 63 (1) (2022) 19-43. https://doi.org/10.1007/s13366-021-00568-1

[47] P. Kumar, S. Pellegrino, Computation of kinematic paths and bifurcation points. International Journal of Solids and Structures. 37 (46) (2000) 7003-7027. 1 https://doi.org/10.1016/S0020-

7683(99)00327-3

[48] Y. Chen, Z. You, Two-fold symmetrical 6R foldable frame and its bifurcations. International Journal of Solids and Structures. 46 (25-26) (2009) 4504-4514. https://doi.org/10.1016/j.ijsolstr.2009.09.012

[49] Y. Chen, P. Sareh, J. Yan, A.S. Fallah, J. Feng, An integrated geometric-graph-theoretic approach to representing origami structures and their corresponding truss frameworks. Journal of Mechanical Design. 141 (9) (2019) 91402. https://doi.org/10.1115/1.4042791

[50] Y. Chen, J. Yan, J. Feng, P. Sareh, Particle swarm optimization-based metaheuristic design generation of non-trivial flat-foldable origami tessellations with degree-4 vertices. Journal of Mechanical Design. 143 (1) (2020) 11703. https://doi.org/10.1115/1.4047437

[51] Y. Chen, C. Lu, J. Yan, J. Feng, P. Sareh, Intelligent computational design of scalene-faceted flat-foldable tessellations. Journal of Computational Design and Engineering. 9 (5) (2022) 1765-1774. https://doi.org/10.1093/jcde/qwac082

[52] T. Yu, J.A. Hanna, Bifurcations of buckled, clamped anisotropic rods and thin bands under lateral end translations. Journal of the Mechanics and Physics of Solids. 122 (2019) 657-685. https://doi.org/10.1016/j.jmps.2018.01.015

[53] W. Huang, Y. Wang, X. Li, M.K. Jawed, Shear induced supercritical pitchfork bifurcation of pre-buckled bands, from narrow strips to wide plates. Journal of the Mechanics and Physics of Solids. 145 (2020) 104168. https://doi.org/10.1016/j.jmps.2020.104168

[54] T.J. Healey, A group-theoretic approach to computational bifurcation problems with symmetry. Computer Methods in Applied Mechanics and Engineering. 67 (3) (1988) 257-295. https://doi.org/10.1016/0045-7825(88)90049-7

[55] J.C. Wohlever, T.J. Healey, A group theoretic approach to the global bifurcation analysis of an axially compressed cylindrical shell. Computer Methods in Applied Mechanics and Engineering. 122 (3-4) (1995) 315-349. https://doi.org/10.1016/0045-7825(94)00734-5

[56] A. Kaveh, M. Nikbakht, Improved group-theoretical method for eigenvalue problems of special symmetric structures, using graph theory. Advances in Engineering Software. 41 (1) (2010) 22-31. https://doi.org/10.1016/j.advengsoft.2008.12.003

[57] S.D. Guest, P.W. Fowler, Symmetry conditions and finite mechanisms. Journal of Mechanics of Materials and Structures. 2 (2) (2007) 293-302. edselc.2-52.0-34548542010 https://doi.org/10.2140/jomms.2007.2.293

[58] Y. Chen, J. Feng, Q. Sun, Lower-order symmetric mechanism modes and bifurcation behavior of deployable bar structures with cyclic symmetry. International Journal of Solids and Structures. 139 (2018) 1-14. https://doi.org/10.1016/j.ijsolstr.2017.05.008

[59] Y. Chen, Q. Sun, J. Feng, Group-theoretical form-finding of cable-strut structures based on irreducible representations for rigid-body translations. International Journal of Mechanical Sciences. 144 (2018) 205-215. https://doi.org/10.1016/j.ijmecsci.2018.05.057

[60] E.T. Filipov, K. Liu, T. Tachi, M. Schenk, G.H. Paulino, Bar and hinge models for scalable analysis of origami. International Journal of Solids and Structures. 124 (2017) 26-45. https://doi.org/10.1016/j.ijsolstr.2017.05.028

[61] K. Liu, G.H. Paulino, Nonlinear mechanics of non-rigid origami: an efficient computational approach. Proceedings of the Royal Society A: Mathematical Physical and Engineering Sciences. 473 (2206) (2017) 20170348. https://doi.org/10.1098/rspa.2017.0348

[62] A. Zingoni, Group-theoretic exploitations of symmetry in computational solid and structural

mechanics. International Journal for Numerical Methods in Engineering. 79 (3) (2009) 253-289. https://doi.org/10.1002/nme.2576

[63] A. Zingoni, On the best choice of symmetry group for group-theoretic computational schemes in solid and structural mechanics. Computers & Structures. 223 (2019) 106101. https://doi.org/10.1016/j.compstruc.2019.106101

[64] K. Ikeda, K. Murota, Bifurcation analysis of symmetric structures using block-diagonalization. Computer Methods in Applied Mechanics and Engineering. 86 (2) (1991) 215-243. https://doi.org/10.1016/0045-7825(91)90128-S

[65] Y. Chen, P. Sareh, J. Feng, Q. Sun, A computational method for automated detection of engineering structures with cyclic symmetries. Computers & Structures. 191 (2017) 153-164. https://doi.org/10.1016/j.compstruc.2017.06.013

[66] Y. Chen, J. Feng, Generalized eigenvalue analysis of symmetric prestressed structures using group theory. Journal of Computing in Civil Engineering. 26 (4) (2012) 488-497. 1 https://doi.org/10.1061/(ASCE)CP.1943-5487.0000151

[67] Y. Chen, L. Fan, Y. Bai, J. Feng, P. Sareh, Assigning mountain-valley fold lines of flat-foldable origami patterns based on graph theory and mixed-integer linear programming. Computers & Structures. 239 (2020) 106328. https://doi.org/10.1016/j.compstruc.2020.106328

[68] P. Zhang, W. Fan, Y. Chen, J. Feng, P. Sareh, Structural symmetry recognition in planar structures using convolutional neural networks. Engineering Structures. 260 (2022) 114227. https://doi.org/10.1016/j.engstruct.2022.114227

[69] S. Lyu, B. Qin, H. Deng, X. Ding, Origami-based cellular mechanical metamaterials with tunable Poisson's ratio: construction and analysis. International Journal of Mechanical Sciences. 212

(2021) 106791. https://doi.org/10.1016/j.ijmecsci.2021.106791

[70] E. Jalali, H. Soltanizadeh, Y. Chen, Y.M. Xie, P. Sareh, Selective hinge removal strategy for architecting hierarchical auxetic metamaterials. Communications Materials. 3 (1) (2022) 97. https://doi.org/10.1038/s43246-022-00322-7